Accepted Manuscript

Ternary assembly of g-C_3N_4/graphene oxide sheets /$BiFeO_3$ heterojunction with enhanced photoreduction of Cr(VI) under visible-light irradiation

Xinjiang Hu, Weixuan Wang, Guangyu Xie, Hui Wang, Xiaofei Tan, Qi Jin, Daixi Zhou, Yunlin Zhao

PII: S0045-6535(18)32052-6

DOI: https://doi.org/10.1016/j.chemosphere.2018.10.181

Reference: CHEM 22443

To appear in: *ECSN*

Received Date: 19 August 2018

Revised Date: 13 October 2018

Accepted Date: 26 October 2018

Please cite this article as: Hu, X., Wang, W., Xie, G., Wang, H., Tan, X., Jin, Q., Zhou, D., Zhao, Y., Ternary assembly of g-C_3N_4/graphene oxide sheets /$BiFeO_3$ heterojunction with enhanced photoreduction of Cr(VI) under visible-light irradiation, *Chemosphere* (2018), doi: https://doi.org/10.1016/j.chemosphere.2018.10.181.

Ternary assembly of g-C_3N_4/graphene oxide sheets /$BiFeO_3$ heterojunction with enhanced photoreduction of Cr(VI) under visible-light irradiation

Xinjiang Hu[a,b], Weixuan Wang[a], Guangyu Xie[a], Hui Wang[a,b,c*], Xiaofei Tan[d,e], Qi Jin[a], Daixi Zhou[a], Yunlin Zhao[a,b,*]

[a] College of Environmental Science and Engineering, Central South University of Forestry and Technology, Changsha 410004, P.R. China.

[b] Faculty of Life Science and Technology, Central South University of Forestry and Technology, Changsha 410004, P.R. China

[c] Institute of Bast Fiber Crops, Chinese Academy of Agricultural Sciences, Changsha, 410205, P.R. China.

[d] College of Environmental Science and Engineering, Hunan University, Changsha 410082, P.R. China.

[e] Key Laboratory of Environmental Biology and Pollution Control (Hunan University), Ministry of Education, Changsha 410082, P.R. China.

Corresponding author: Hui Wang, Yunlin Zhao

E-mail addresses: wanghuii623@163.com (H. Wang), zyl8291290@163.com (Y. Zhao)

Abstract:

A novel ternary composite of graphitic carbon nitride (g-C_3N_4) / graphene oxide (GO) sheets / $BiFeO_3$ (CNGB) with highly enhanced visible-light photocatalytic activity toward Cr(VI) photoreduction is prepared and characterized. The characterization and photocatalysis experiments corroborate its reasonable band gap, efficient charge separation and transfer, widened visible-light adsorption, easy solid-liquid separation, good stability and superior catalytic activity of CNGB. Three CNGB samples with different ratios of g-C_3N_4 and $BiFeO_3$ (CNGB-1, -2, -3 with 2:4, 3:3, and 4:2, respectively), though possessing different adsorption ability, eventually remove all Cr(VI) ions via photocatalysis within 90 min. The catalytic efficiency of the composite is the highest at pH 2; increases in pH decrease the catalytic ability. The inorganic anions such as SO_4^-, Cl^-, and NO_3^- only slightly affects the photocatalytic process. The matching of the band structure between $BiFeO_3$ and g-C_3N_4 generates efficient photogenerated electron migration from the conduction band of g-C_3N_4 to that of $BiFeO_3$, which is also facilitated by the electron bridging and collecting effects of GO, and holes transfer from the valence band of $BiFeO_3$ to that of g-C_3N_4, yielding the efficient separation of photogenerated electron-hole pairs and the subsequent enhancement of photocatalytic activity. The research provides a theoretical basis and technical support for the development of photocatalytic technologies for effective application in wastewater treatment and Cr-contaminated water restoration.

Keywords: g-C_3N_4 nanosheets; $BiFeO_3$; Cr(VI) photoreduction; Heterojunction; Electrolyte ion

1 Introduction

Cr is a common pollutant in industrial wastewaters produced by tanning, printing and dyeing, and the fabrication of medicine and preservatives (Mondal et al., 2014; Huang et al., 2015; Liu et al., 2015b). As Cr-polluted wastewater is highly toxic and complex in chemical composition, its pollution control has become an important part of water treatment research. In water, Cr exists in the two main states of trivalent Cr(III) and hexavalent Cr(VI) (Kim and Choi, 2011). Their morphological distributions not only determine their behavioral characteristics and toxicities in different media, but also affects their treatment methods (Li et al., 2015). Cr(VI) is both mobile and highly toxic (Wang et al., 2014), while Cr(III) is a necessary trace element of the human body 100 times less toxic than Cr(VI); it can be removed from water by the simple methods of precipitation and adsorption [7, 8]. Therefore, the typical process for treating Cr(VI) is reducing Cr(VI) to low-toxicity Cr(III) and then removing Cr(III) by precipitation (Kim and Choi, 2011; Liu et al., 2014a; Huang et al., 2015). Photocatalysis is an environmentally friendly technology that effectively reduces Cr(VI) to Cr(III) (Abdullah and Kuo, 2015). In this process, the photocatalyst determines the catalytic efficiency, so it is important to find efficient photocatalysts for removing Cr(VI) from wastewater.

In recent years, g-C_3N_4, a metal-free polymeric photocatalyst with a visible-light-region bandgap and proper band edges, has been introduced in the field of photocatalytic treatment and has attracted widespread attention (Fresno et al., 2014; Zhao et al., 2015). The C and N atoms in the g-C_3N_4 structure are sp^2-hybridized, forming a highly delimited π-conjugated system (Shen et al., 2015). The N p_z and C p_z orbits form the highest occupied molecular orbital (HOMO) and the lowest unoccupied molecular orbital (LUMO), with the band positions of +1.4 eV and -1.3 eV relative to a normal hydrogen electrode (NHE), respectively

(Liu et al., 2015a). The standard reduction potential of Cr(VI)/Cr(III) is +1.38 eV, below the g-C_3N_4 conduction band (CB). Therefore, from a thermodynamic perspective, the use of g-C_3N_4 for reducing Cr(VI) to Cr (III) is feasible (Zhang et al., 2015).

However, the application of g-C_3N_4 in the field of photocatalytic treatment retains the following two problems: First, the quantum efficiency is low because of the high recombination rate of photogenerated electron-hole pairs. To improve the photocatalytic activity of g-C_3N_4, many new materials have been prepared, such as Ag-$Sr_{0.25}H_{1.5}Ta_2O_6 \cdot H_2O$/g-$C_3N_4$ (Xin et al., 2016), g-C_3N_4-TiO_2 (Sridharan et al., 2013; Thankam Thomas and Sandhyarani, 2015), g-C_3N_4/ZnO (Liu et al., 2012), F-g-C_3N_4 (Dong and Zhang, 2013) and F¯doping ultrathin g-C_3N_4 (Li et al., 2018b). Second, g-C_3N_4 is difficult to separate and recycle from solutions. Usually, the specific surface area is inversely proportional to the particle size. Thus, the particle size of g-C_3N_4 is minimized to increase its specific surface area and thus improve its catalytic efficiency. The separation of catalysts and the purification processes for catalytic systems are complex and costly. For this reason, some magnetic materials, such as Fe_3O_4 (Zhou et al., 2013) and α-Fe_2O_3 (Xiao et al., 2015), have been composited with g-C_3N_4 to improve the solid-liquid separation ability of the photocatalyst.

$BiFeO_3$, with a relatively narrow band gap (~2.2 eV), has both ferroelectric and antiferromagnetic properties, as well as photocatalytic abilities under visible-light irradiation (Wang et al., 2015; Sharma et al., 2016). Coupling $BiFeO_3$ with g-C_3N_4 can form a new composite. The magnetic material provides an effective solution of the problem of photocatalyst recovery. In addition, the matching band potentials between $BiFeO_3$ and g-C_3N_4 permit easy migration of the photoinduced electrons in g-C_3N_4 to $BiFeO_3$. The new routes for photogenerated electron-hole pairs can suppress electron-hole recombination in the hybrid composite photocatalyst, ensuring higher efficiency of the electron-hole pairs (Wang et al.,

2015). However, the direct coupling of g-C_3N_4 with $BiFeO_3$ may limit electron transfer.

Graphene oxide, with its 2D ultra-thin carbon nanostructure and large specific surface area, is an ideal nanomaterial as a scaffold carrying nanomaterials on its nanosheets (Min and Lu, 2011). Moreover, its excellent electrical conductivity can facilitate electrons storage and charge transport in the photocatalysis system(Jiang et al., 2011; Zhao et al., 2013; Hu et al., 2016). Utilized as a scaffold carrying g-C_3N_4 and $BiFeO_3$, the GO can provide a path or a sink for charge migration and collection, enhancing electron transfer and utilization efficiency and electron-hole recombination. Meanwhile, GO can provide many active sorption sites owing to a large amount of oxygen-containing functional groups in its structure, namely hydroxyl, carboxyl, and epoxy groups (Chen et al., 2015). Therefore, the coupling of g-C_3N_4, $BiFeO_3$ and GO to form a ternary heterogeneous material may simultaneously solve the above two problems, thus promoting the application of g-C_3N_4-based materials in the field of photocatalysis.

There are different views on the reduction mechanism of Cr(VI) by g-C_3N_4-based materials. Most studies suggest that Cr(VI) is converted directly into Cr (III) by photogenerated electrons (Sridharan et al., 2013; Xin et al., 2016). Hu et al. (2014b) attributed the reduction of Cr(VI) to the direct transfer of photogenerated electrons and the indirect transfer of electrons by $\bullet O_2^-$. In addition, the study by Dong and Zhang (2013) showed that F-g-C_3N_4 formed by fixing the formate anion on the surface of g-C_3N_4 could change the surface potential and increase the adsorption of Cr(VI) ions. The F-g-C_3N_4 could also change $\bullet O_2^-$-mediated indirect reduction to direct photogenerated electron reduction, thereby improving the Cr(VI) photoreduction. Likewise, Wei et al. (2016) also reported that hydrothermally treated g-C_3N_4 in HNO_3 aqueous solution could induce one-step Cr(VI) reduction directly by electrons owing to the change of its surface chemistry.

In summary, although many studies on the photocatalytic treatment of Cr(VI) have been conducted, the photocatalytic mechanism of Cr(VI) on the surface of g-C_3N_4-based materials requires further study. In this study, magnetically responsive $BiFeO_3$ was coupled with monolayer GO and g-C_3N_4 to form a g-C_3N_4/GO/$BiFeO_3$ ternary coupling material (CNGB), which has the characteristics of good stability, a reasonable band gap, high catalytic activity, easy solid-liquid separation, and good visible-light response. The effects of environmental conditions on the photoreduction of Cr(VI) by the CNGB were studied, and the microscopic mechanism of Cr(VI) photoreduction was deeply investigated. This study has important practical significance for improving the efficiency of Cr-contaminated wastewater treatment.

2 Materials and methods

2.1 Synthesis of CNGB

All chemicals used in this study were analytical-grade reagents. The g-C_3N_4 powders were prepared through the calcination of melamine, in which 30 g of melamine was added to a crucible and washed by ultrapure water and ethanol. Next, the crucible was placed in a muffle furnace and heated at 70 □ for 40 min, then heated at 600 □ for 3 h. The obtained light-yellow materials were ground to obtain g-C_3N_4 powders.

GO was prepared using the modified Hummers method (Yang et al., 2010; Hu et al., 2014a; Hu et al., 2016). Briefly, graphite powders were firstly pre-oxidized by $K_2S_2O_8$, P_2O_5, and concentrated sulfuric acid to obtain pre-oxidized graphite. Then, the pre-oxidized graphite was deeply oxidized by concentrated sulfuric acid, $NaNO_3$, and $KMnO_4$ at different temperatures. Next, the graphite oxide layers were separated from each other by ultrasonication to obtain the GO suspension.

The $BiFeO_3$ was prepared by the sol-gel process (Luo et al., 2010), in which 0.08 mol

ferric nitrate and 0.08 mol bismuth nitrate were dissolved in 200 mL of 2-methoxyethanol, and then 0.2 mL of 0.1 mol/L nitric acid was added. In 100 mL of ethylene glycol, 0.08 mol citric acid was dissolved, and this solution was added to the above mixture. The solution was heated and stirred at 60 °C for 1 h, and then heated at 100 °C for 10 h to obtain a light-yellow gel. The resulting gel was poured into a crucible and heated at 200 °C for 30 min, then calcined at 500 °C for 2 h. The product was cooled and ground to obtain the $BiFeO_3$.

The typical preparation of CNGB photocatalysts was as follows (Wang et al., 2015): appropriate amounts of these synthesized g-C_3N_4 (3 g), GO (0.5 g), and $BiFeO_3$ (3 g) powders were firstly dispersed in 100 mL methanol assisted by ultrasonication for 3 h at 50 □. After volatilization of the methanol in a fume hood and drying at 80 □ for 6 h, the CNGB powder (CNGB-2) was obtained. Another two CNGB composite samples with different mass ratios of g-C_3N_4, GO, and $BiFeO_3$ (CNGB-1, 2:0.5:4; CNGB-3, 4:0.5:2) were prepared according to the methods described above.

2.2 Characterization

The phase compositions of the materials were analyzed by X-ray diffraction (XRD) using a D/max-2500 (Rigaku, Japan) diffractometer with Cu Kα radiation. The microstructural morphologies of the materials were characterized by a QUANTA250 field-emission scanning electron microscope (FE-SEM; FEI, USA). The surface elements were analyzed using ESCALAB 250Xi X-ray photoelectron spectroscopy (XPS; Thermo Fisher Scientific, USA). The magnetic properties of the sample were measured by a MPMS-XL-7 vibrating-sample magnetometer (VSM; Quantum Design Instruments, USA). The samples were analyzed by a NICOLET 5700 Fourier-transform infrared spectroscope

(FTIR; Thermo Nicolet Corporation, USA). Photoluminescence (PL) spectra were recorded on a FLS 980 fluorescence spectrophotometer (Edinburgh Instruments, UK). Thermogravimetric (TG) curves were obtained using a SDT Q600 thermal analyzer (TA, USA) in atmospheric conditions from room temperature to 1000 °C (flux rate 100 mL/min, heating rate 10 °C/min). Ultraviolet-visible (UV-vis) diffuse reflectance spectra (DRS) of the samples were recorded on a U-4100 UV-vis diffuse reflection spectrophotometer (Hitachi, Japan) using $BaSO_4$ as the reference. The electron spin resonance (ESR) signals of the spin-trapped radicals were examined on a JES FA200 spectrometer (JEOL, Japan) using the spin-trapping reagent 5,5-dimethyl-1-pyrroline *N*-oxide (DMPO) under visible light irradiation.

2.3 Photoelectrochemical measurements

The experiments were performed on a CHI 660D workstation with a three-electrode model, namely the counter, reference and working electrode (Deng et al., 2017). An Ag/AgCl electrode soaked in KCl solutions and a Pt electrode were used as the reference and counter electrode, respectively. The working electrodes were fabricated as below. 0.02 g of prepared sample was dispersed in 2 mL 0.25% Nafion solution through ultrasonic dispersion for at least 30 min. Then, 0.1 mL of aforementioned solution was dropped onto a 1 cm × 2 cm FTO substrate. Next, the extra part was scratched using a blade to ensure the available surface area of 1.0 cm^2 on the FTO substrate. Three electrodes were placed in a 0.5 M sodium sulfate electrolyte solution with a 300 W Xe lamp equipped with a UV cutoff filter illuminating the coated samples to form a photoelectrochemical test system. Electrochemical impedance spectroscopy (EIS) was similarly performed on an Autolab workstation (AUT85812) using abovementioned three-electrode model.

2.4 Photocatalytic activity test

The photocatalytic performances of the samples toward the photoreduction of Cr(VI) were tested under visible light irradiation. A 300 W Xe lamp (CEL-HXF300, Beijing China Education Au-light Co. Ltd) equipped with a UV cutoff filter ($\lambda > 400$ nm) was chosen as a visible light source. Briefly, 200 mL of a 5 mg/L Cr(VI) solution was added to a beaker, and the solution pH was adjusted to the desired value by adding 0.01 or 0.1 M NaOH and HCl solution. Then, 0.5 g samples of the as-prepared catalysts were added into the Cr(VI) solutions. The resulting suspensions were magnetically stirred for 1 h in darkness to establish the equilibrium of Cr(VI) adsorption-desorption on the photocatalyst surfaces before irradiation. At given time intervals, 5 mL samples of the suspensions were taken from the beakers and filtered through 0.45-μm membrane filters for analysis. The concentration of Cr(VI) ions in the samples was determined by a UV spectrophotometer at 540 nm.

3 Results and discussion

3.1 Characterizations

3.1.1 SEM

The morphologies of the as-prepared g-C_3N_4, $BiFeO_3$, and CNGB-2 were investigated by SEM, and the results are shown in Fig. 1. As can be seen from Fig. 1a, the g-C_3N_4 appears to form aggregated particles containing many irregular smaller crystals (Liu et al., 2012). From Fig. 1b, the $BiFeO_3$ are composed of fine particles with grain sizes of approximately 100 nm. For the CNGB-2 heterojunctions (Fig. 1c and d), the introduction of g-C_3N_4 and GO causes interesting changes in the morphology of $BiFeO_3$. The GO sheets have typical fabric-like shapes and crumpled nanostructures, while the g-C_3N_4 has a layered structure with a few

208 stacking layers (Wang et al., 2015). The $BiFeO_3$ nanoparticles are randomly distributed on the

209 surfaces of the GO and g-C_3N_4 sheets.

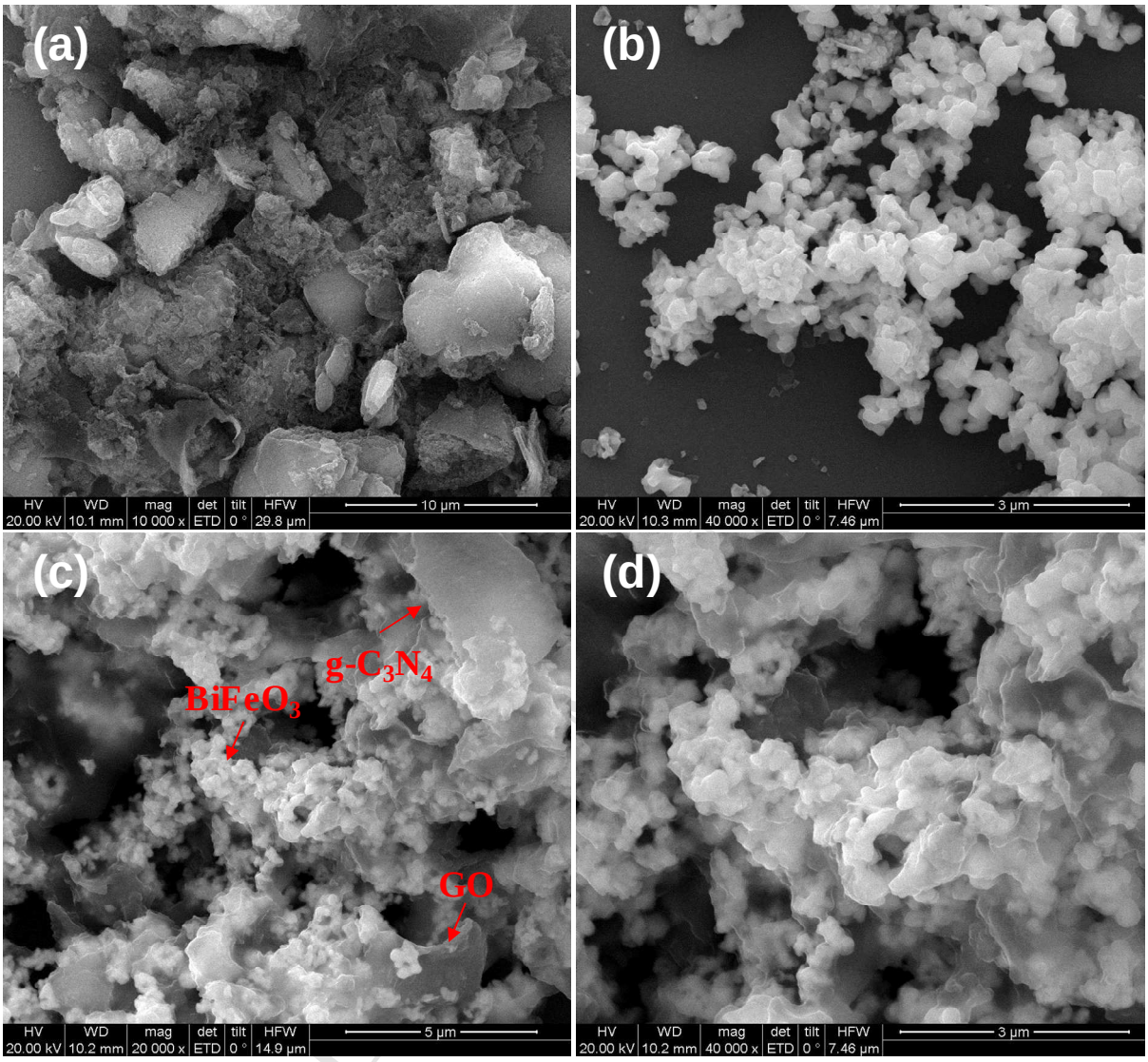

210

211

212 Fig. 1. SEM images of (a) g-C_3N_4, (b) $BiFeO_3$, (c) and (d) CNGB-2 heterojunctions.

213 3.1.2 XPS

214 To study the binding states and the elemental compositions of the as-prepared g-C_3N_4,

215 $BiFeO_3$, and CNGB heterojunctions, XPS analysis has been conducted (Fig. 2). As shown in

216 Fig. 2a, the survey XPS spectrum of CNGB shows that the main elements of the prepared

217 samples are Bi, O, Fe, C, and N. As reported in our previous study (Hu et al., 2016), the main

elements of GO are C and O. Therefore, C in the heterojunctions mainly originates from g-C_3N_4 and GO, while O mainly originates from $BiFeO_3$ and GO. The C 1*s* XPS spectrum of the CNGB-2 obtained at high resolution is demonstrated in Fig. 2b. This spectrum can be curve-fitted into five different peaks at 284.42, 284.61, 285.30, 286.90, 288.01, and 289.0 eV, corresponding to C–C (in GO), C–N (in g-C_3N_4), C–O (in GO), C–O–C (in GO), N–C=N (in g-C_3N_4) or C=O (in GO), and O–C=O (in GO) groups, respectively (Ma et al., 2012; Shen et al., 2015; Hu et al., 2016; Wang et al., 2016). From Fig. 2c, the O 1*s* characteristic peaks at 529.81, 530.50, 532.45, and 533.28 eV are attributable to the Bi–O (in $BiFeO_3$), C=O (in GO), C–O (in GO), and O–C=O (in GO) groups, respectively (Deng et al., 2017; Wang et al., 2017). From Fig. 2d, the binding energies of N 1*s* at 398.49 and 400.24 eV can be assigned to N atoms sp^2-bonded to two carbon atoms (C–N=C) and bridging nitrogen atoms N-$(C)_3$, respectively (Xiao et al., 2015; Wang et al., 2016). From Fig. 2e, the Bi 4*f* spectrum is deconvoluted into two peaks at approximately 159.23 and 164.54 eV, corresponding to the binding energies of Bi $4f_{7/2}$ and Bi $4f_{5/2}$, respectively (Wang et al., 2017).

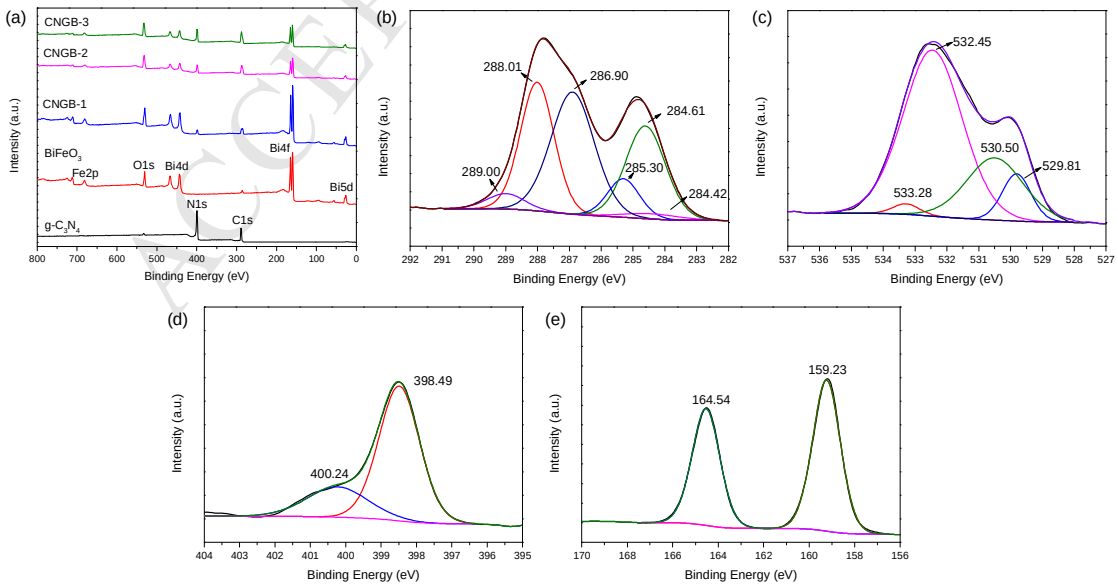

Fig. 2 (a) XPS survey spectra of g-C_3N_4, $BiFeO_3$, and CNGB heterojunctions; High-resolution spectra of (b) C 1*s*, (c) O 1*s*, (d) N 1*s*, (e) Bi 4*f* of CNGB-2 heterojunction.

3.1.3 XRD

Fig. S1 shows the XRD patterns of the g-C_3N_4, $BiFeO_3$, and CNGB heterojunctions. From g-C_3N_4, two diffraction peaks are located at 13.0° and 27.4°, which can be ascribed to the (100) and (102) diffraction planes of g-C_3N_4 (JCPDS 87-1526) (Xiao et al., 2015). For the $BiFeO_3$, many major peaks are observed and can be assigned to diffractions from the (012), (104), (110), (006), (202), (024), (116), (122), (018), (202), (214), (300), (208), and (220) planes of the single-phase perovskite structure of $BiFeO_3$ (JCPDS Card No. 20-169) (Luo et al., 2010). In the XRD patterns of CNGB-1, CNGB-2, and CNGB-3, the major peaks of both g-C_3N_4 (JCPDS 87-1526) and $BiFeO_3$ (JCPDS Card No. 20-169) are seen, confirming that the synthesized CNGB heterojunctions contain different amounts of g-C_3N_4 and the $BiFeO_3$.

3.1.4 FTIR

Fig. S2 shows the FTIR spectra of the g-C_3N_4, $BiFeO_3$, GO, and CNGB heterojunctions. For g-C_3N_4, the absorption peak at around 808 cm^{-1} is attributed to the out-of-plane bending modes of C-N heterocycles (Kang et al., 2012). The peaks observed in the range of 1200-1600 cm^{-1} correspond to typical aromatic C-N stretching vibrations (Zhang et al., 2015). The peak at 1639 cm^{-1} is ascribed to C=N stretching vibration (Su et al., 2015). As for $BiFeO_3$, two strong peaks are observed at 438 and 552 cm^{-1}, corresponding to the O-Fe-O bending vibrations and the Fe-O stretching of FeO_6 groups in $BiFeO_3$, respectively (Luo et al., 2010). The characteristic peaks of GO appear at 1103 cm^{-1} (C–O), 1396 cm^{-1} (C–OH), 1628 cm^{-1} (C=C in the aromatic ring), and 1718 cm^{-1} (C=O groups) (Zhao et al., 2011; Ma et al., 2012).

All peaks of g-C_3N_4, $BiFeO_3$, and GO are also present in the FTIR spectra of the CNGB heterojunctions, which further indicates that the g-C_3N_4 and GO are successfully combined with $BiFeO_3$ (An et al., 2016).

3.1.5 VSM

To study the magnetic properties of CNGB-2, the magnetization hysteresis curves of $BiFeO_3$ and CNGB-2 were measured using VSM (Fig. S3). The magnetic hysteresis loops are S-like curves. The saturation magnetization (M_s), coercivity (H_c) and retentivity (M_r) are 2.95 emu/g, 75.22 Oe, and 0.28 emu/g for $BiFeO_3$, and 1.45 emu/g, 47.53 Oe, and 0.10 emu/g for CNGB-2, respectively. Both samples have near-zero retentivities, indicating that the magnetization almost disappears when the external magnetic field is removed. The $BiFeO_3$ and CNGB-2 exhibit superparamagnetic behaviors at room temperature (Hu et al., 2014a), which is important for the convenient recycling of these heterojunctions. After the photocatalytic process is completed, the CNGB-2 can be collected from the aqueous solution by a magnet and the clear solution can be decanted off (Hu et al., 2014a).

3.2 Investigation on charge separation and optical properties.

Serving as a charge bridge, GO can promote electron transfer from CBs of g-C_3N_4 to $BiFeO_3$ and holes in turn from VBs of $BiFeO_3$ to g-C_3N_4 in the process of visible-light photocatalysis, thereby inhibiting the recombination of the photogenerated carriers (An et al., 2016). It is confirmed through the comparison of charge separation properties among g-C_3N_4, g-C_3N_4-$BiFeO_3$, and CNGB-2. PL spectroscopy is widely used to investigate the separation efficiency of the photogenerated carriers in photocatalysis. Higher PL signals indicate lower separation efficiencies for the photogenerated electrons and holes (Deng et al., 2017). Fig. 3a

shows the PL spectra of g-C_3N_4 and CNGB-2 heterojunctions at the excitation wavelength of 400 nm. The g-C_3N_4 and g-C_3N_4-$BiFeO_3$ show comparatively strong PL intensity, while the CNGB-2 heterojunction has a much lower PL signal. The results confirm lower recombination probability of free charges in the CNGB-2 than other prepared samples by employing GO nanosheet as a charge bridge between g-C_3N_4 and $BiFeO_3$. The charge-transfer-bridge effect of GO can be further corroborated by the photocurrent-time (I-t) curves in Fig. 3b which demonstrates better photocurrent response of CNGB-2 than g-C_3N_4-$BiFeO_3$ and g-C_3N_4. EIS measurement shows the photogenerated charge transfer at solid/bulk interfaces and smaller arc radius can represent lower charge transfer resistance (Li et al., 2018a) . Obviously, as shown in Fig 3c, the diameter of arc radius lies in the order CNGB-2> g-C_3N_4-$BiFeO_3$> g-C_3N_4, confirming that CNGB-2 heterojunction exhibits greater charge separation and interfacial charge transfer than other pure or binary composite materials.

The optical properties determine the ability of a photocatalytic material to absorb light. Therefore, the optical properties of the g-C_3N_4, $BiFeO_3$, and CNGB heterojunctions were investigated and the results are shown in Fig. 3d. From Fig. 3d, the g-C_3N_4 sample has a sharp absorption edge at ~460 nm, attributed to the intrinsic band gap of g-C_3N_4(Wen et al., 2016). $BiFeO_3$ shows an absorption edge at 642 nm. Compared to the g-C_3N_4 sample, the adsorption band edge of the CNGB heterojunctions is slightly red-shifted under visible light, indicating that the absorption of CNGB heterojunctions shifts to a lower-energy region. By coupling $BiFeO_3$ with g-C_3N_4, the photocatalyst can absorb more visible light to generate electron-hole pairs, thereby improving the photocatalytic efficiency (Wang et al., 2015). The band gaps of

299 g-C_3N_4 and $BiFeO_3$ are estimated as 2.70 eV and 1.93 eV, respectively. The energy levels of
300 g-C_3N_4 and $BiFeO_3$ were calculated using the Mulliken electronegativity theory (Fan et al.,
301 2015; Liu et al., 2017). The CBs of g-C_3N_4 and $BiFeO_3$ are located at −1.13 eV and +0.58 eV,
302 respectively. The valence bands (VBs) of g-C_3N_4 and $BiFeO_3$ are at +1.57 eV and +2.51 eV,
303 respectively. The band gap of pure g-C_3N_4 and $BiFeO_3$ are narrowed by coupling them on GO
304 to form CNGB, among which CNGB-2, with the ratio of g-C_3N_4 and $BiFeO_3$ at 1:1, possesses
305 the lowest band gap energy.

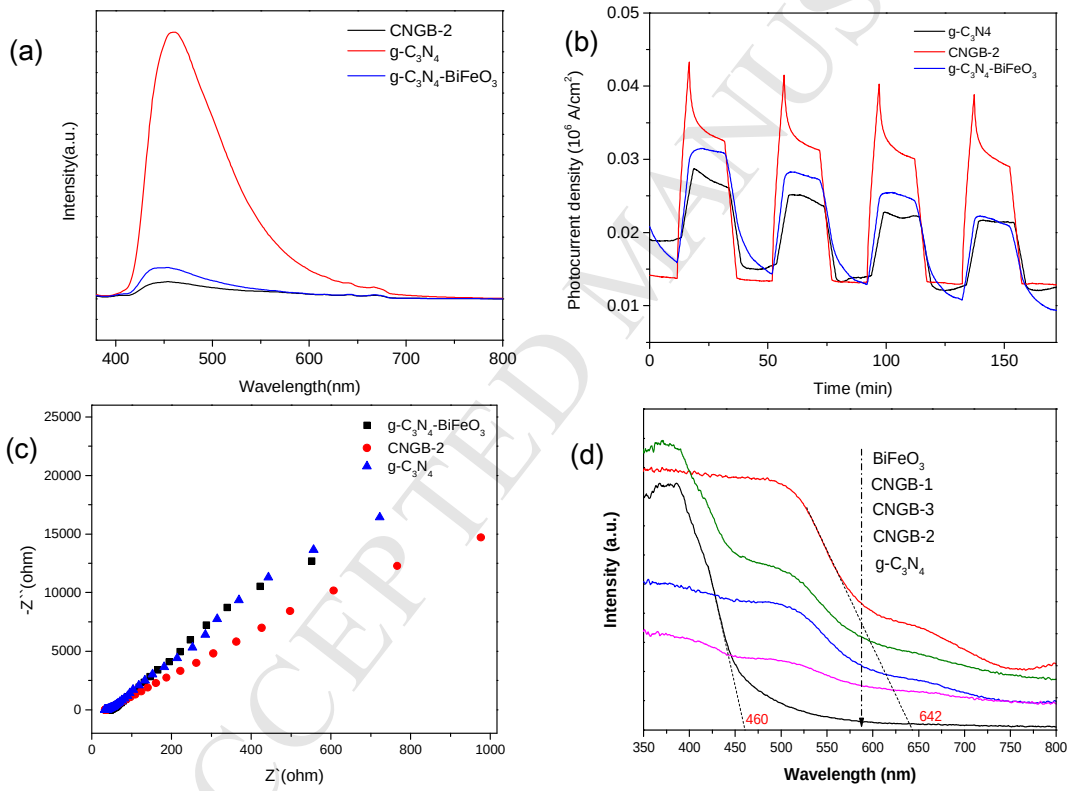

306
307 Fig.3 (a) Photoluminescence spectra, (b) Photocurrent response density, (c) EIS Nyquist plots
308 of g-C_3N_4, g-C_3N_4-$BiFeO_3$ and CNGB-2 , (d) UV-vis spectra g-C_3N_4, $BiFeO_3$, and CNGB-1,
309 2, 3.

310 **3.3 Photoreduction of Cr(VI)**

311 In order to evaluate the photocatalytic capability of the prepared CNGB heterojunctions,

Cr(VI) was selected as the target contaminant. Considering the characteristics of wastewater, the material preparation process was firstly optimized, and the influences of pH and competing ions on the photocatalytic process were studied. Furthermore, the recycling performance of the CNGB heterojunctions was also investigated.

3.3.1 Optimization of CNGB heterojunctions

Fig. 4a illustrates the photocatalytic activities of g-C_3N_4, $BiFeO_3$, and CNGB heterojunctions with different mass ratios for Cr(VI) in aqueous solution under visible light irradiation. We can see that the g-C_3N_4 only remove 14% of Cr(VI) by adsorption after 60 min. After irradiation with visible light, the Cr(VI) is gradually reduced; the removal efficiency reaches 95% after 240 min. In the adsorption period, $BiFeO_3$ has a larger adsorption capacity for Cr(VI) ions than g-C_3N_4, with approximately 36% Cr(VI) removal after 1 h. When the system is irradiated with visible light, the photocatalytic reduction rate of Cr(VI) is low and the removal rate of Cr(VI) reaches only 54% after 240 min. However, the photocatalytic properties of CNGB are much better than those of pure g-C_3N_4 and $BiFeO_3$. From Fig. 4a, the CNGB-1 has the largest adsorption capacity for Cr(VI), while Cr(VI) can be completely reduced by all three kinds of CNGB heterojunctions within 90 min. This means that the different ratios of g-C_3N_4 and $BiFeO_3$ only affect the interaction of the photocatalyst with the Cr(VI) ions, without significantly affecting the removal process of Cr(VI). The CNGB-2 was used as the photocatalyst in the following experiments.

3.3.2 Effect of pH

The solution pH is important in the photocatalytic process because it affects the aqueous chemistry and the surface potential of the photocatalyst. In general, the pH range of

wastewater is relatively wide (Hu et al., 2014a). Therefore, the influence of the pH on the photocatalytic process requires study. Fig. 4b shows the effect of the initial solution pH on Cr(VI) ion removal by the CNGB-2 heterojunction. We can see that the pH value has a great influence on the removal process. When the pH value is 2, 100% of Cr(VI) ions are removed within 120 min, and the removal rates are decreased continuously with increasing pH value. When the pH value is 8, only 35% of Cr(VI) ions is reduced. The Cr(VI) speciation (5 mg/L) as a function of pH value, as calculated by the visual MINTEQ program, is illustrated in Fig. 4c. Under different pH conditions, Cr(VI) ions exist in different forms such as CrO_4^{2-}, H_2CrO_4(aq), $Cr_2O_7^-$, and $HCrO_4^-$ (Hu et al., 2018). When 2.0 < pH < 6.0, $HCrO_4^-$ is the dominant form of Cr(VI). When pH > 6, the main form of Cr(VI) ions is CrO_4^{2-}. Compared with neutral and alkaline solutions, $HCrO_4^-$ is more easily captured by the CNGB-2 heterojunction and abundant H^+ promote its reduction by the photogenerated electrons. The photocatalytic reduction of Cr(VI) occurs as follows (Liu et al., 2014a):

$$HCrO_4^- + 7H^+ + 3e_{cb}^- \rightarrow Cr^{3+} + 4H_2O \quad (1)$$

We can see that the acidic medium is beneficial for Cr(VI) reduction because of the existence of abundant H^+(Fida et al., 2015) (Liu et al., 2014a). Under high-pH conditions, the capture of CrO_4^{2-} is difficult because of the electrostatic repulsion between the CNGB-2 heterojunction and Cr(VI), and Cr(VI) does not react easily with the photogenerated electrons, thereby decreasing the Cr(VI) removal rate (Hu et al., 2018).

3.3.3 Effect of competing ions

Cr-containing industrial wastewaters often contain many electrolyte ions (Liu et al., 2015b), which can affect the species of Cr ions and the chemical characteristics of the water

environment [40] and further influence the migration, transformation, and regression of Cr ions. The electrolyte ions in the solution also affect the photocatalysis of Cr(VI) ions. Therefore, the effects of Na_2SO_4, $NaNO_3$, and $CaCl_2$ on the photoreduction of Cr(VI) by the CNGB-2 heterojunction were investigated in this study, and the results are shown in Fig. 4d. No significant effects of $NaNO_3$ and $CaCl_2$ are observed. In the adsorption stage, the Cr(VI) adsorption is significantly inhibited by adding Na_2SO_4, mainly because of the competition of SO_4^{2-} with the Cr(VI) ions for adsorption on the binding sites on the surfaces of the CNGB-2 heterojunction (Hu et al., 2018). In the photocatalytic process, Cr(VI) is still completely reduced within 100 min in the presence of Na_2SO_4, indicating that Na_2SO_4 has less effect on the photocatalytic process. This may be because the SO_4^{2-} in the solution can react with some of photogenerated electrons to generate SO_4^{-}•, and then the electrons can be transferred indirectly to Cr(VI).

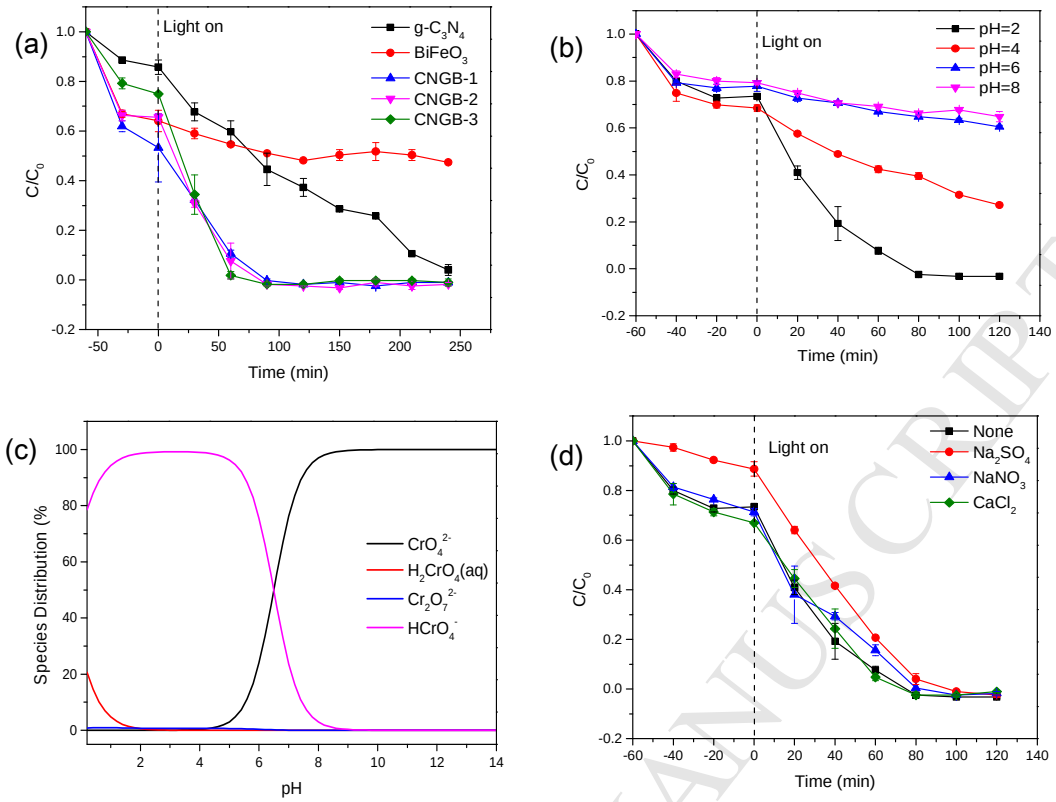

Fig. 4 (a) Photoreduction of Cr(VI) by g-C_3N_4, $BiFeO_3$, and CNGB heterojunctions under visible light irradiation: $C_{0Cr(□)}$= 5 mg/L, m/V = 2.5 g/L, pH = 2.0, (b) Effect of pH values on the photoreduction of Cr(VI) with CNGB-2 heterojunction: $C_{0Cr(□)}$= 5 mg/L, m/V = 2.5 g/L, (c) Distribution of Cr(VI) species computed by visual MINTEQ at different pH values, (d) Effect of 25 mM competing ions on the photoreduction of Cr(VI) by CNGB-2 heterojunction under visible light irradiation: $C_{0Cr(□)}$ = 5 mg/L, m/V = 2.5 g/L, pH = 2.0.

3.3.4 Reuse of CNGB-2

In order to determine the practicability and recyclability of the CNGB-2 heterojunction, recycling experiments were performed and the results are demonstrated in Fig. S4. After the first cycle, the CNGB-2 heterojunctions were recovered, washed, and dried, and then used in a second cycle. The recycling experiments were performed three times. As can be seen from Fig. S4, the adsorption capacity is reduced slightly, possibly because the oxygen-containing

groups on the surface of GO reacts with free radicals, thereby decreasing the binding sites available for Cr(VI) ions in the next cycle (Wang et al., 2013). We also find that the photocatalytic performance of the CNGB-2 heterojunctions shows no significant decrease after three cycles.

3.4 Possible photocatalytic reaction mechanism

3.4.1 Roles of reactive species

In order to study the main active species in solution for Cr(VI) reduction during the photocatalytic reaction and to understand the reaction mechanism in depth, three typical scavengers of *tert*-butyl alcohol (TBA, 10 mM), $K_2S_2O_8$ (10 mM), and ethylenediaminetetraacetic acid disodium (EDTA-2Na, 10 mM) were added to the photocatalytic systems as quenchers of radicals (•OH), electrons (e^-), and holes (h^+), respectively. As shown in Fig. 5, the addition of 10 mM TBA causes almost no change in the photoreduction of Cr(VI), indicating that the highly oxidizing •OH is not the main reactive species inhibiting the photoreduction of Cr(VI). When $K_2S_2O_8$ is added into the photocatalytic system, the photoreduction of Cr(VI) over the CNGB-2 heterojunction is significantly decreased, implying that the photogenerated electrons are a dominant reaction species in Cr(VI) reduction. The photocatalytic reduction of Cr(VI) is dramatically improved by adding EDTA-2Na, which may be because the reaction of EDTA-2Na with photogenerated holes hinders the recombination of photogenerated electrons and holes (Xiao et al., 2015).

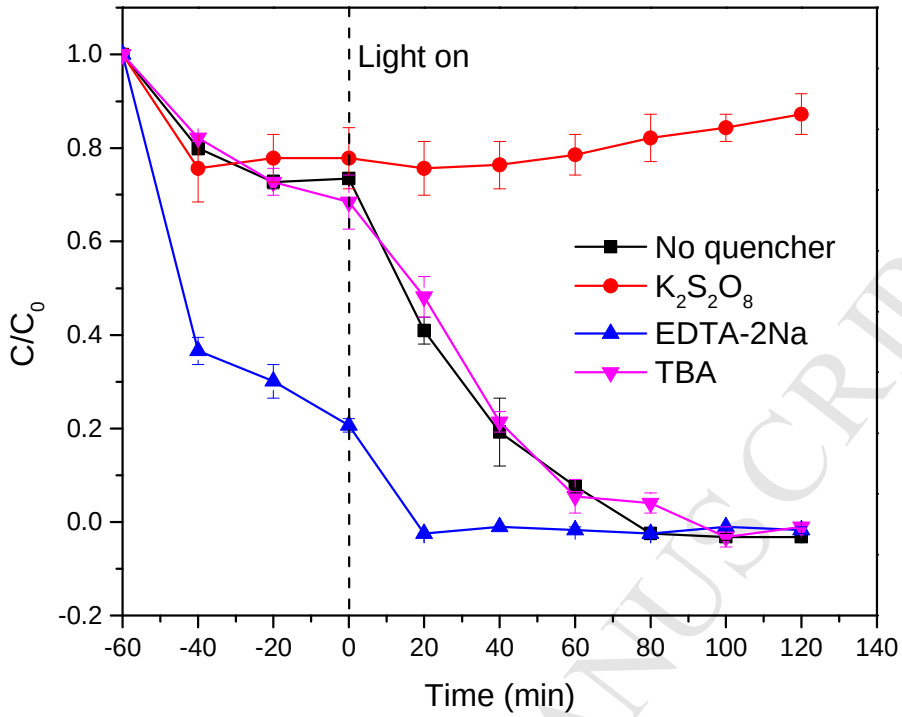

Fig. 5 Trapping experiments for the photoreduction of Cr(VI) over CNGB-2 heterojunction under visible light irradiation: $C_{0Cr(□)}$ = 5 mg/L, m/V = 2.5 g/L, pH = 2.0.

The roles of the active species in the photoreduction of Cr(VI) are further confirmed by the ESR technique in Fig. S5. No obvious signals of DMPO-•O_2^- and DMPO-•OH are observed under dark conditions for the CNGB-2 heterojunction. However, notable signals of DMPO-•O_2^- and DMPO-•OH are observed after the systems are irradiated under visible light for 5 and 10 min, indicating that •O_2^- and •OH are produced during the photocatalytic reaction (Wan et al., 2017). Because the redox potential value of OH^-/•OH (+2.40 eV) is slightly lower than VBs of $BiFeO_3$ (+2.51 eV), H_2O or OH^- can serve as hole scavengers and react with holes on VB of $BiFeO_3$ to produce •OH (Liu et al., 2014b) (Deng et al., 2017). Likewise, the producing of •O_2^- is ascribed to the reaction between dissolved O_2 and photoinduced electrons on CB of g-C_3N_4 because the redox potential value of O_2/•O_2^- at -0.33

413 eV is lower than CB of g-C_3N_4 at -1.33 eV (Deng et al., 2017). This process not only
414 consumes photoexcited holes through the reaction of holes with H_2O to produce •OH but also
415 induces a •O_2^--mediated Cr(VI) photoreduction, thereby increasing the separation efficiency
416 of the photogenerated charge carriers and accelerating the photoreduction of Cr(VI) (Dong
417 and Zhang, 2013).

418 One thing worth mentioning is that the introduction of GO instead decreases the
419 generating amount of •OH, as is illustrated in Fig. S6. The possible explanation is that the
420 existence of GO that is rich in various oxygen-containing functional groups enhances the
421 adsorption of Cr(VI) on the surface or interface of CNGB-2 so that there are less chance for
422 H_2O or OH^- to be captured by holes on its surface, compared with the photocatalysis system
423 with g-C_3N_4-$BiFeO_3$. As a result, although CNGB-2 produces less radicals but more Cr(VI)
424 ions tend to be captured onto the active sites of CNGB-2 and reduced directly by its electrons
425 whether collected on GO nanosheets or accumulated on the conduction band of $BiFeO_3$.

426 3.4.2 Mechanisms of enhanced photocatalytic performance

427 Fig. 6 shows the possible mechanism of generation, transfer, and reaction of the
428 photoelectron-hole pairs. In the photocatalytic reaction system, both g-C_3N_4 and $BiFeO_3$ can
429 be excited by visible light to generate photoelectrons and holes. The photogenerated electrons
430 can transfer from the CB of g-C_3N_4 to that of $BiFeO_3$, because of the difference between the
431 CB edge potentials of g-C_3N_4 and $BiFeO_3$ at -1.33 and +0.58 eV, respectively (Fan et al.,
432 2015). GO can act as an electron sink in collecting and delivering electrons, thereby
433 facilitating the charge transfer and separation from holes. Hence, the Cr(VI) ions adsorbed on
434 CNGB-2 are reduced to Cr(III) by the electrons dispersed on the surfaces of GO nanosheets.

435 Meanwhile, the photoinduced holes can be migrated from VB of $BiFeO_3$ to that of g-C_3N_4 as
436 a result of the matching of VBs edge potentials of g-C_3N_4 and $BiFeO_3$ at 1.57 and 2.51 eV,
437 respectively (Fan et al., 2015). As photogenerated holes are retained on the VB of g-C_3N_4 and
438 photoinduced electrons accumulate on the CB of $BiFeO_3$, the recombination of
439 photoelectron-hole pairs is largely inhibited. Photogenerated electrons on CBs of g-C_3N_4
440 partly react with O_2 to form $\bullet O_2^-$ which is believed to be a mediator to reduce Cr(VI) (Dong
441 and Zhang, 2013). And the photoexcited holes are consumed by H_2O or OH^- to produce •OH
442 which is proved to play a minor role in oxidizing Cr(III) back into Cr(VI), further
443 strengthening the electron-hole separation and improving Cr(VI) decontamination efficiency.
444 The combined effects of effective visible-light utilization, high separation rate of
445 photoelectron-hole pairs and accelerated charge transfer contribute to high-efficiency
446 photocatalytic reduction capacity (Deng et al., 2017).

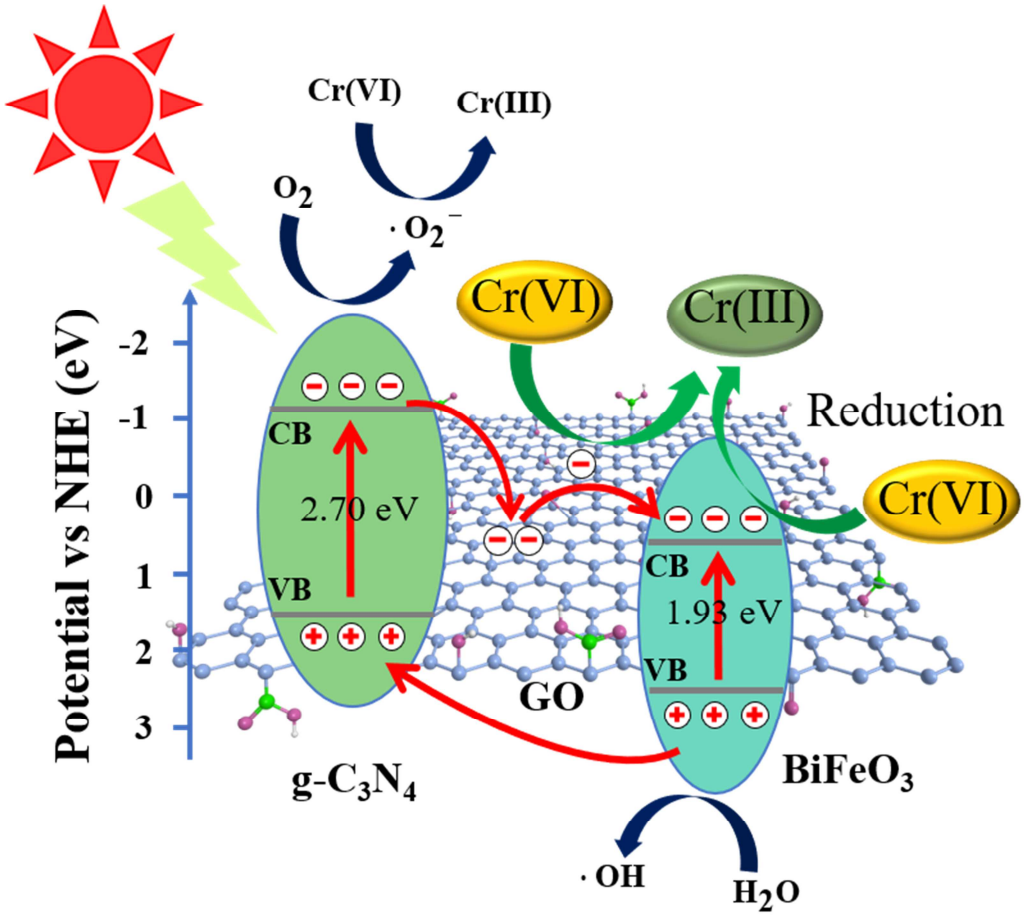

Fig. 6 Illustration of possible mechanism for Cr(VI) photoreduction over CNGB-2 heterojunction under visible light irradiation.

XPS analysis was performed on the CNGB-2 heterojunction after the photocatalytic reaction, and the results are shown in Fig. S7. As is seen from Fig. S7a, the XPS survey spectrum of CNGB-2 after irradiation shows a small Cr peak around 580 eV. From Fig. S7b, after Cr(VI) adsorption, both Cr(III) and Cr(VI) exist on the surface of the heterojunction. The O 1*s* XPS spectrum demonstrated in Fig. S7c can be deconvoluted into four different peaks at 529.97, 531.32, 532.06, and 532.99 eV, respectively, which are different from those observed before the photocatalytic reaction. This may be because some oxygen-containing groups on the surface of GO reacts with the free radical and some react with the Cr(III) and Cr(VI) ions. Based on these results, a degradation mechanism for Cr(VI) can be proposed. Firstly, the

negatively charged Cr(VI) is adsorbed by the CNGB-2, and then the adsorbed Cr(VI) ions are reduced to Cr(III) ions by electrons photogenerated by the CNGB-2 (Fida et al., 2015). Finally, the Cr(III) ions are captured by the heterojunction.

4 Conclusions

A g-C_3N_4/GO/$BiFeO_3$ ternary coupling material (CNGB) was prepared using a simple method. The optical and photoelectrochemical measurement collaborated greatest visible light adsorption and charge transfer on the interface and surface of CNGB-2. The CNGB also achieved high catalytic efficiency, a reasonable band gap, good visible-light response, easy separation from treated water, recyclability and stability. From batch experiments, three CNGB heterojunctions with different ratios of g-C_3N_4 and $BiFeO_3$ (CNGB-1, -2, and -3 with 2:4, 3:3, and 4:2, respectively) all exhibited complete removal of Cr(VI) ions. The catalytic efficiency of the composite was maximized at pH 2. The inorganic anions such as NO_3^-, Cl^-, and SO_4^{2-}, though affecting a bit the adsorption capacity, were found to exert neglectable influences on final removal of Cr(VI) through photocatalysis. The recycling experiments demonstrated that CNGB maintains great catalytic performance after three cycles. The lower chance of electron-hole pairs recombination and improved photocatalytic efficiency were ascribed to an effective electron transfer path provided by CNGB-2 and broadened visible-light adsorption. In the photocatalysis system, the production of •OH were found to scarcely suppress the photoreduction of Cr(VI) but the generated $\cdot O_2^-$ can donate electrons to Cr(VI) so as to mediate the photoreduction process. It is believed that CNGB is an effective candidate for the remediation of Cr-contaminated wastewater.

Acknowledgements

This study was financially supported by the National Natural Science Foundation of China (Grant No. 51608208), the Natural Science Foundation of Hunan Province (Grant No. 2018JJ3887 and 2018JJ3096), the China Postdoctoral Science Foundation (Grant No. 2017M610513), the Research Foundation of Education Department of Hunan Province, China (Grant No. 17K105), the Natural Science Foundation of Guangdong Province (Grant No. 2016A030310246 and 2016A030310456), the Science and Technology Planning Project of Hunan Province (Grant No. 2016TP2007 and 2016TP1014), and the Scientific Research Staring Foundation for the attracted talent of Central South University of Forestry and Technology (Grant No. 2016YJ001).

References

Abdullah, H., Kuo, D.H., 2015. Facile Synthesis of n-type (AgIn)x$Zn_{2(1-x)}S_2$/p-type Ag_2S Nanocomposite for Visible Light Photocatalytic Reduction To Detoxify Hexavalent Chromium. Acs Appl Mater Interfaces 7, 26941-26951.

An, J., Zhang, G., Zheng, R., Wang, P., 2016. Removing lignin model pollutants with $BiFeO_3$–g-C_3N_4 compound as an efficient visible-light-heterogeneous Fenton-like catalyst. Journal of Environmental Sciences 48, 218-229.

Chen, H., Gao, B., Li, H., 2015. Removal of sulfamethoxazole and ciprofloxacin from aqueous solutions by graphene oxide. Journal of hazardous materials 282, 201-207.

Deng, Y., Tang, L., Zeng, G., Feng, C., Dong, H., Wang, J., Feng, H., Liu, Y., Zhou, Y., Pang, Y., 2017. Plasmonic resonance excited dual Z-scheme $BiVO_4$/Ag/Cu_2O nanocomposite:

synthesis and mechanism for enhanced photocatalytic performance in recalcitrant antibiotic degradation. Environ. Sci.: Nano 4, 1494-1511.

Dong, G., Zhang, L., 2013. Synthesis and Enhanced Cr(VI) Photoreduction Property of Formate Anion Containing Graphitic Carbon Nitride. The Journal of Physical Chemistry C 117, 4062-4068.

Fan, T., Chen, C., Tang, Z., Ni, Y., Lu, C., 2015. Synthesis and characterization of g-C_3N_4/$BiFeO_3$ composites with an enhanced visible light photocatalytic activity. Mater Sci Semicon Process 40, 439-445.

Fida, H., Guo, S., Zhang, G., 2015. Preparation and characterization of bifunctional Ti-Fe kaolinite composite for Cr(VI) removal. Journal of colloid and interface science 442, 30-38.

Fresno, F., Portela, R., Suárez, S., Coronado, J.M., 2014. Photocatalytic materials: recent achievements and near future trends. Journal of Materials Chemistry A 2, 2863-2884.

Hu, X.-j., Liu, Y.-g., Zeng, G.-m., Wang, H., Hu, X., Chen, A.-w., Wang, Y.-q., Guo, Y.-m., Li, T.-t., Zhou, L., Liu, S.-h., Zeng, X.-x., 2014a. Effect of aniline on cadmium adsorption by sulfanilic acid-grafted magnetic graphene oxide sheets. J Colloid Interface Sci 426, 213-220.

Hu, X., Ji, H., Chang, F., Luo, Y., 2014b. Simultaneous photocatalytic Cr(VI) reduction and 2,4,6-TCP oxidation over g-C_3N_4 under visible light irradiation. Catalysis Today 224, 34-40.

Hu, X., Wang, H., Liu, Y., 2016. Statistical Analysis of Main and Interaction Effects on Cu(II) and Cr(VI) Decontamination by Nitrogen-Doped Magnetic Graphene Oxide. Scientific reports 6, 34378.

Hu, X., Zhao, Y., Wang, H., Cai, X., Hu, X., Tang, C., Liu, Y., Yang, Y., 2018. Decontamination of Cr(VI) by graphene oxide@TiO_2 in an aerobic atmosphere: effects of

pH, ferric ions, inorganic anions, and formate. Journal of Chemical Technology & Biotechnology.

Huang, B., Liu, Y., Li, B., Zeng, G., Hu, X., Zheng, B., Li, T., Jiang, L., Tan, X., Zhou, L., 2015. Synthesis of graphene oxide decorated with core@double-shell nanoparticles and application for Cr(VI) removal. RSC Advances 5, 106339-106349.

Jiang, B., Tian, C., Pan, Q., Jiang, Z., Wang, J.-Q., Yan, W., Fu, H., 2011. Enhanced Photocatalytic Activity and Electron Transfer Mechanisms of Graphene/TiO_2 with Exposed {001} Facets. The Journal of Physical Chemistry C 115, 23718-23725.

Kang, H.W., Lim, S.N., Song, D., Park, S.B., 2012. Organic-inorganic composite of g-C_3N_4–$SrTiO_3$:Rh photocatalyst for improved H_2 evolution under visible light irradiation. International Journal of Hydrogen Energy 37, 11602-11610.

Kim, K., Choi, W., 2011. Enhanced redox conversion of chromate and arsenite in ice. Environ Sci Technol 45, 2202-2208.

Li, H., Wu, T., Cai, B., Ma, W., Sun, Y., Gan, S., Han, D., Niu, L., 2015. Efficiently photocatalytic reduction of carcinogenic contaminant Cr (VI) upon robust AgCl:Ag hollow nanocrystals. Applied Catalysis B: Environmental 164, 344-351.

Li, J., Wang, J., Zhang, G., Li, Y., Wang, K., 2018a. Enhanced molecular oxygen activation of Ni^{2+} -doped BiO_{2-x} nanosheets under UV, visible and near-infrared irradiation: Mechanism and DFT study. Applied Catalysis B: Environmental 234, 167-177.

Li, J., Zhao, W., Wang, J., Song, S., Wu, X., Zhang, G., 2018b. Noble metal-free modified ultrathin carbon nitride with promoted molecular oxygen activation for photocatalytic formaldehyde oxidization and DFT study. Applied Surface Science 458, 59-69.

Liu, J., Liu, Y., Liu, N., Han, Y., Zhang, X., Huang, H., Lifshitz, Y., Lee, S.-T., Zhong, J., Kang, Z., 2015a. Metal-free efficient photocatalyst for stable visible water splitting via a two-electron pathway. Science 347, 970-974.

Liu, W., Cao, L., Cheng, W., Cao, Y., Liu, X., Zhang, W., Mou, X., Jin, L., Zheng, X., Che, W., Liu, Q., Yao, T., Wei, S., 2017. Single-site active cobalt-based photocatalyst with long carriers lifetime for spontaneous overall water splitting. Angewandte Chemie (International ed. in English).

Liu, W., Ni, J., Yin, X., 2014a. Synergy of photocatalysis and adsorption for simultaneous removal of Cr(VI) and Cr(III) with TiO_2 and titanate nanotubes. Water Res 53, 12-25.

Liu, W., Ni, J., Yin, X., 2014b. Synergy of photocatalysis and adsorption for simultaneous removal of Cr(VI) and Cr(III) with TiO_2 and titanate nanotubes. Water Res 53, 12-25.

Liu, W., Wang, M., Xu, C., Chen, S., 2012. Facile synthesis of g-C_3N_4/ZnO composite with enhanced visible light photooxidation and photoreduction properties. Chem Eng J 209, 386-393.

Liu, Y., Mou, H., Chen, L., Mirza, Z.A., Liu, L., 2015b. Cr(VI)-contaminated groundwater remediation with simulated permeable reactive barrier (PRB) filled with natural pyrite as reactive material: Environmental factors and effectiveness. J Hazard Mater 298, 83-90.

Luo, W., Zhu, L., Wang, N., Tang, H., Cao, M., She, Y., 2010. Efficient Removal of Organic Pollutants with Magnetic Nanoscaled $BiFeO_3$ as a Reusable Heterogeneous Fenton-Like Catalyst. Environmental Science & Technology 44, 1786-1791.

Ma, H.L., Zhang, Y.W., Hu, Q.H., Yan, D., Yu, Z.Z., Zhai, M.L., 2012. Chemical reduction and removal of Cr(VI) from acidic aqueous solution by ethylenediamine-reduced graphene

567 oxide. J Mater Chem 22, 5914-5916.

568 Min, S., Lu, G., 2011. Dye-Sensitized Reduced Graphene Oxide Photocatalysts for Highly
569 Efficient Visible-Light-Driven Water Reduction. The Journal of Physical Chemistry C 115,
570 13938-13945.

571 Mondal, C., Ganguly, M., Pal, J., Roy, A., Jana, J., Pal, T., 2014. Morphology controlled
572 synthesis of SnS_2 nanomaterial for promoting photocatalytic reduction of aqueous Cr(VI)
573 under visible light. Langmuir 30, 4157-4164.

574 Sharma, S., Saravanan, P., Pandey, O.P., Vinod, V.T.P., Černík, M., Sharma, P., 2016.
575 Magnetic behaviour of sol–gel driven $BiFeO_3$ thin films with different grain size distribution.
576 Journal of Magnetism and Magnetic Materials 401, 180-187.

577 Shen, C., Chen, C., Wen, T., Zhao, Z., Wang, X., Xu, A., 2015. Superior adsorption capacity
578 of g-C_3N_4 for heavy metal ions from aqueous solutions. Journal of colloid and interface
579 science 456, 7-14.

580 Sridharan, K., Jang, E., Park, T.J., 2013. Novel visible light active graphitic C_3N_4–TiO_2
581 composite photocatalyst: Synergistic synthesis, growth and photocatalytic treatment of
582 hazardous pollutants. Applied Catalysis B: Environmental 142-143, 718-728.

583 Su, Y., Zhao, Y., Zhao, Y., Lang, J., Xin, X., Wang, X., 2015. Novel ternary component
584 Ag-$SrTa_2O_6$/g-C_3N_4 photocatalyst: Synthesis, optical properties and visible light
585 photocatalytic activity. Appl Surf Sci 358, 213-222.

586 Thankam Thomas, R., Sandhyarani, N., 2015. Template free synthesis of graphitic carbon
587 nitride/titania mesoflowers. RSC Advances 5, 72683-72690.

588 Wan, Z., Zhang, G., Wu, X., Yin, S., 2017. Novel visible-light-driven Z-scheme

$Bi_{12}GeO_{20}$/g-C_3N_4 photocatalyst: Oxygen-induced pathway of organic pollutants degradation and proton assisted electron transfer mechanism of Cr(VI) reduction. Applied Catalysis B-Environmental 207, 17-26.

Wang, H., Liu, Y.-g., Zeng, G.-m., Hu, X.-j., Hu, X., Li, T.-t., Li, H.-y., Wang, Y.-q., Jiang, L.-h., 2014. Grafting of β-cyclodextrin to magnetic graphene oxide via ethylenediamine and application for Cr(VI) removal. Carbohydr Polym 113, 166-173.

Wang, H., Yuan, X., Wang, H., Chen, X., Wu, Z., Jiang, L., Xiong, W., Zeng, G., 2016. Facile synthesis of Sb_2S_3/ultrathin g-C_3N_4 sheets heterostructures embedded with g-C_3N_4 quantum dots with enhanced NIR-light photocatalytic performance. Applied Catalysis B: Environmental 193, 36-46.

Wang, J., Tang, L., Zeng, G., Deng, Y., Liu, Y., Wang, L., Zhou, Y., Guo, Z., Wang, J., Zhang, C., 2017. Atomic scale g-C_3N_4/Bi_2WO_6 2D/2D heterojunction with enhanced photocatalytic degradation of ibuprofen under visible light irradiation. Applied Catalysis B-Environmental 209, 285-294.

Wang, P., Wang, J., Ming, T., Wang, X., Yu, H., Yu, J., Wang, Y., Lei, M., 2013. Dye-sensitization-induced visible-light reduction of graphene oxide for the enhanced TiO_2 photocatalytic performance. Acs Appl Mater Interfaces 5, 2924-2929.

Wang, X., Mao, W., Zhang, J., Han, Y., Quan, C., Zhang, Q., Yang, T., Yang, J., Li, X., Huang, W., 2015. Facile fabrication of highly efficient g-C_3N_4/$BiFeO_3$ nanocomposites with enhanced visible light photocatalytic activities. J Colloid Interface Sci 448, 17-23.

Wei, H., Zhang, Q., Zhang, Y., Yang, Z., Zhu, A., Dionysiou, D.D., 2016. Enhancement of the Cr(VI) adsorption and photocatalytic reduction activity of g-C_3N_4 by hydrothermal treatment

in HNO_3 aqueous solution. Applied Catalysis a-General 521, 9-18.

Wen, M.Q., Xiong, T., Zang, Z.G., Wei, W., Tang, X.T., Dong, F., 2016. Synthesis of MoS_2/g-C_3N_4 nanocomposites with enhanced visible-light photocatalytic activity for the removal of nitric oxide (NO). Optics Express 24.

Xiao, D., Dai, K., Qu, Y., Yin, Y., Chen, H., 2015. Hydrothermal synthesis of α-Fe_2O_3/g-C_3N_4 composite and its efficient photocatalytic reduction of Cr(VI) under visible light. Applied Surface Science 358, 181-187.

Xin, X., Lang, J., Wang, T., Su, Y., Zhao, Y., Wang, X., 2016. Construction of novel ternary component photocatalyst $Sr_{0.25}H_{1.5}Ta_2O_6 \cdot H_2O$ coupled with g-C_3N_4 and Ag toward efficient visible light photocatalytic activity for environmental remediation. Applied Catalysis B: Environmental 181, 197-209.

Yang, S.T., Chang, Y.L., Wang, H.F., Liu, G.B., Chen, S., Wang, Y.W., Liu, Y.F., Cao, A.N., 2010. Folding/aggregation of graphene oxide and its application in Cu^{2+} removal. J Colloid Interface Sci 351, 122-127.

Zhang, Y., Zhang, Q., Shi, Q., Cai, Z., Yang, Z., 2015. Acid-treated g-C_3N_4 with improved photocatalytic performance in the reduction of aqueous Cr(VI) under visible-light. Sep Purif Technol 142, 251-257.

Zhao, G.X., Li, J.X., Ren, X.M., Chen, C.L., Wang, X.K., 2011. Few-layered graphene oxide nanosheets as superior sorbents for heavy metal ion pollution management. Environ Sci Technol 45, 10454-10462.

Zhao, Y., Zhao, D., Chen, C., Wang, X., 2013. Enhanced photo-reduction and removal of Cr(VI) on reduced graphene oxide decorated with TiO_2 nanoparticles. J Colloid Interface Sci

405, 211-217.

Zhao, Z., Sun, Y., Dong, F., 2015. Graphitic carbon nitride based nanocomposites: a review. Nanoscale 7, 15-37.

Zhou, X., Jin, B., Chen, R., Peng, F., Fang, Y., 2013. Synthesis of porous Fe_3O_4/g-C_3N_4 nanospheres as highly efficient and recyclable photocatalysts. Mater Res Bull 48, 1447-1452.

Highlights

1. g-C_3N_4/graphene oxide/$BiFeO_3$(CNGB) ternary assembly is easily prepared.

2. CNGB shows excellent photocatalysis of Cr(□) reduction and easy removal from water.

3. CNGB shows maximized efficiency at low pH.

4. CNGB have little chance of electron-hole recombination.

5. CNGB shows great visible-light response.